Supporting Information

For

Sulfur-Containing Analogs of the Reactive $[CuOH]^{2+}$ Core

Wen Wu,[a] Jacqui Tehranchi De Hont,[b] Riffat Parveen,[c] Bess Vlaisavljevich,[c,*] and William B. Tolman[a,*]

a Department of Chemistry, Washington University in St. Louis, One Brookings Hall, Campus Box 1134, St. Louis, MO 63130-4899.
b Department of Chemistry, University of Minnesota, 207 Pleasant Ave SE, Minneapolis, MN 55455.
c University of South Dakota, 414 E Clark St. Vermillion, SD 57069.

*Corresponding authors: wbtolman@wustl.edu, bess.vlaisavljevich@usd.edu

Table of Contents

1. Experimental materials and methods

General Methods. All syntheses were carried out under nitrogen, using conventional glovebox or standard Schlenk techniques. Tetrahydrofuran (THF), diethyl ether and acetonitrile were purified with a dual column Solv-Tek solvent purification system, plumbed directly into the glovebox, and stored over 3 Å molecular sieves. All the solvents were passed through basic alumina prior to use. Compounds LCu(CH_3CN),[1] LCuCl, [1] Bu_4NSH, [2] TEMPOH, [3] and $FcBAr^F$ [4] were synthesized according to literature procedures. All other reagents and solvents were purchased from commercial sources and used as received. UV-vis spectra were obtained using an HP8453 (190-1100) diode array spectrophotometer. Variable temperature UV-vis experiments were performed using a Unisoku low temperature cell holder. Cyclic voltammograms were recorded using an EC Epsilon potentiostat from BASi, a glassy-carbon working electrode, Platinum counter electrode, and a Ag^+/Ag reference electrode. Ferrocene was then added into the solution as internal standard and the final potentials were converted vs. the standard Fc^+/Fc couple. [5] EPR spectra were recorded on a CW X-band Elexsys E500 EPR spectrometer equipped with an Oxford ESR 910 liquid helium cryostat. All spectra were recorded at a temperature of 30 K and at a microwave frequency of 9.38 GHz under the following conditions: microwave power 0.0002 mW; modulation amplitude 9.8 G; modulation frequency 100 kHz. The simulations of the spectra were performed in Matlab using the program EasySpin.

[Bu_4N][LCuSH] ([Bu_4N][1]). In a glovebox, Bu_4NSH (0.055 g, 0.19 mmol) was added to THF (~2 mL) to give a yellow-green suspension, which was then added dropwise to a stirring solution of LCu(CH_3CN) (0.109 g, 0.19 mmol) in THF (~ 5 mL) to produce a dark purple solution, and allowed to stir for 30 min. The mixture was then filtered, and the solvent was removed from the filtrate in vacuo. The resulting dark purple solid was washed with diethyl ether (3 x 3 mL),

redissolved in THF (~2 mL), and recrystallized by layering with ether (~3 mL), giving dark purple crystalline product (0.094g, 63%). UV-Vis (THF, -80°C), λ_{max}, nm (ε, M^{-1} cm^{-1}): 397 (sh, 3380), 559 (668). EPR, g(x): 2.045; g(y): 2.064, g(z): 2.133. Anal. Calcd for $C_{47}H_{74}CuN_4O_2S$: C, 68.61; H, 9.07; N, 6.81; Found: C, 67.88; H, 9.43; N, 6.62.

Synthesis of LCuSH. For a typical reaction monitored by UV-vis spectroscopy, 4 mM solutions of [Bu_4N][**1**] and $FcBAr^F$ were prepared in THF. A 0.1 mL of the solution of [Bu_4N][**1**] was added to a UV-vis cuvette along with 1.8 mL of THF. After cooling the cuvette to −80 °C, 0.1 mL of the 4 mM $FcBAr^F$ solution was added, causing the immediate formation of an intensely dark blue solution. UV-Vis (THF, -80°C), λ_{max}, nm (ε, M^{-1} cm^{-1}): 582 (6900).

Synthesis of [Bu_4N][LCuSPh] ([Bu_4N][2]). NaSPh (0.022 g, 0.017 mmol) was added to THF (~2mL) to give a colorless solution, and then added dropwise to a stirring green solution of LCuCl (0.140 g, 0.17 mmol) in THF (~ 5 mL) to produce a dark red solution, and allowed to stir for 2 h. The mixture was then filtered, and the solvent was removed in vacuo. The resulting dark purple solid was washed with diethyl ether three times, redissolved in THF, and recrystallized by layering with ether, giving dark red solid (0.112 g, 73%). UV-Vis (THF, -80°C), λ_{max},nm (ε, M^{-1} cm^{-1}): 370 (sh, 7490), 512 (1690). EPR, g(x):2.051; g(y): 2.075; g(z):2.149. Anal. Calcd for $C_{53}H_{78}CuN_4O_2S$: C, 70.82; H, 8.75; N, 6.23; Found: C, 69.11; H, 8.92; N, 6.06.

Synthesis of LCuSPh. For a typical reaction monitored by UV-vis spectroscopy, 2 mM solutions of [Bu_4N][**2**] and $FcBAr^F$ were prepared in THF. A 0.1 mL of the solution of [Bu_4N][**2**] was first added to a UV-vis cuvette along with 1.8 mL of THF. After cooling the cuvette to −80 °C, 0.1 mL of the 2 mM $FcBAr^F$ solution was added, causing the immediate formation of an intensely purple species. UV-Vis (THF, -80°C), λ_{max}, nm (ε, M^{-1} cm^{-1}): 538 (11700).

Preparation of the EPR samples of LCuSH and LCuSPh. In a 2mm EPR tube, 0.1mL of 5mM of [Bu_4N][**1**] or [Bu_4N][**2**] was injected and was cooled to −78 °C in a dry ice/acetone bath. 0.1mL of 5mM of $FcBAr^F$ solution was then added. A total of 0.3 mL of THF solvent was used to rinse the EPR tube between each addition. The solution was mixed and then frozen in liquid nitrogen for analysis. The EPR spectrum of both samples were featureless (silent).

Reactions of LCuSH and LCuSPh with TEMPOH.

At various temperatures (-40 to -80 °C), a solution of [Bu_4N][**1**] (0.1 mL, 4 mM) or [Bu_4N][**2**] (0.1 mL, 2 mM) was added to a UV-vis cuvette containing THF (1.7 mL) and cooled to the desired temperature followed by addition of $FcBAr^F$ in THF (0.1 mL, 4 mM for $\mathbf{1}^-$ and 2 mM for $\mathbf{2}^-$). Subsequently, a solution of TEMPOH in THF (0.1 mL, 10 equiv.) was quickly added with mixing. The reaction was then followed until full decay of the signal at 582 nm for LCuSH or 538 nm for LCuSPh had occurred. The reactions were run in duplicate. Pseudo first-order rate constants (k_{obs}) were determined by fitting plots of absorbance (582 nm for LCuSH and 538nm for LCuSPh) vs. time to a single exponential decay curve. For each experiment, k_{obs} values were averaged. A plot of average k_{obs} vs. [TEMPOH] was fit to a straight line with approximate zero intercept, indicating second order kinetics for the overall reaction with the second order rate law Rate = k[Cu][TEMPOH]. The second order rate constant (k) used in Eyring plot was determined by multiwavelength analysis using ReactLab^{TM} KINETICS. UV-vis spectra were truncated to 450-800 nm for fitting to a second order model.

In order to identify the presumed radical product, in a 2 mm EPR tube, 0.1 mL of 5 mM of [Bu_4N][**1**] was injected and was cooled to −78 °C in a dry ice/acetone bath. To this solution 0.1 mL of 5 mM of $FcBAr^F$ solution was added, and the tube quickly shaken to form a dark blue solution. A solution of TEMPOH in THF (0.1 mL, 50 mM, 10 equiv.) was layered onto the solution

and allowed to thermally equilibrate, and then mixed. A total of 0.2 mL of THF solvent was used to rinse the EPR tube between each addition. After 10 min, the resulting brown solution was frozen in liquid nitrogen for analysis.

2. EPR data for complexes $[Bu_4N][LCu^{II}SH]$ and $[Bu_4N][LCu^{II}SPh]$

(a)

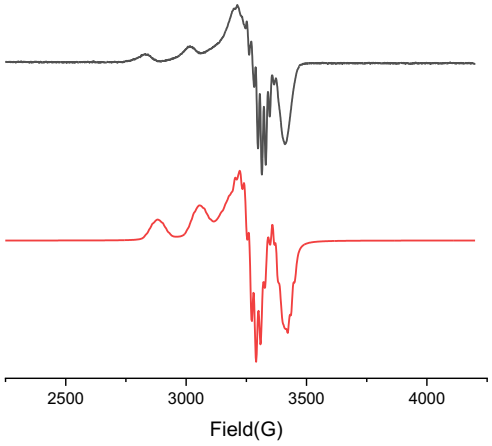

(b)

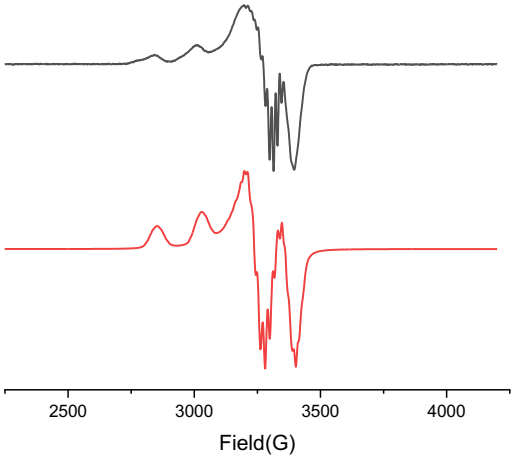

Figure S1. Experimental (black) and simulated (red) X-band EPR spectra of $[Bu_4N][\mathbf{1}]$ (a) and $[Bu_4N][\mathbf{2}]$ (b). The frequencies were 9.379 GHz for (a) and 9.378 GHz for (b).

Table S1. Simulated EPR parameters. Hyperfine parameters (A) given in MHz (numbers in parentheses were converted to $\times 10^{-4}$ cm^{-1})

	$[Bu_4N][\mathbf{1}]$	$[Bu_4N][\mathbf{2}]$
g(x)	2.045	2.051
g(y)	2.064	2.075
g(z)	2.133	2.149
$A^{Cu}(x)$	100 (33.4)	100 (33.4)
$A^{Cu}(y)$	80 (26.7)	80 (26.7)
$A^{Cu}(z)$	515 (172)	530 (177)
$A^{amide}(x)$	55 (18.3)	55 (18.3)
$A^{amide}(y)$	45 (15.0)	40 (13.3)
$A^{amide}(z)$	40 (13.3)	35 (11.7)
$A^{py}(x)$	50 (16.7)	55 (18.3)
$A^{py}(y)$	55 (18.3)	55 (18.3)
$A^{py}(z)$	65 (21.7)	50 (16.7)

3. Cyclic voltammogram data

(a)

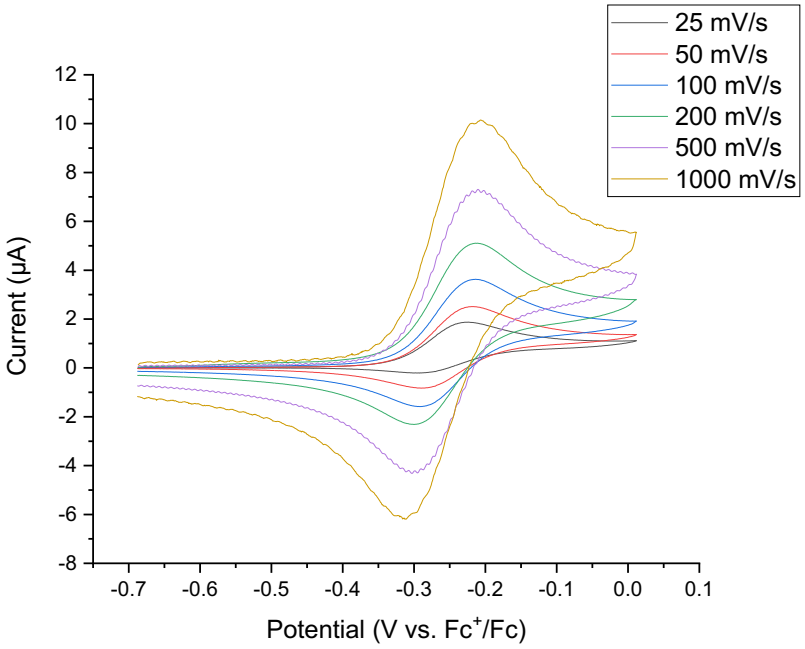

(b)

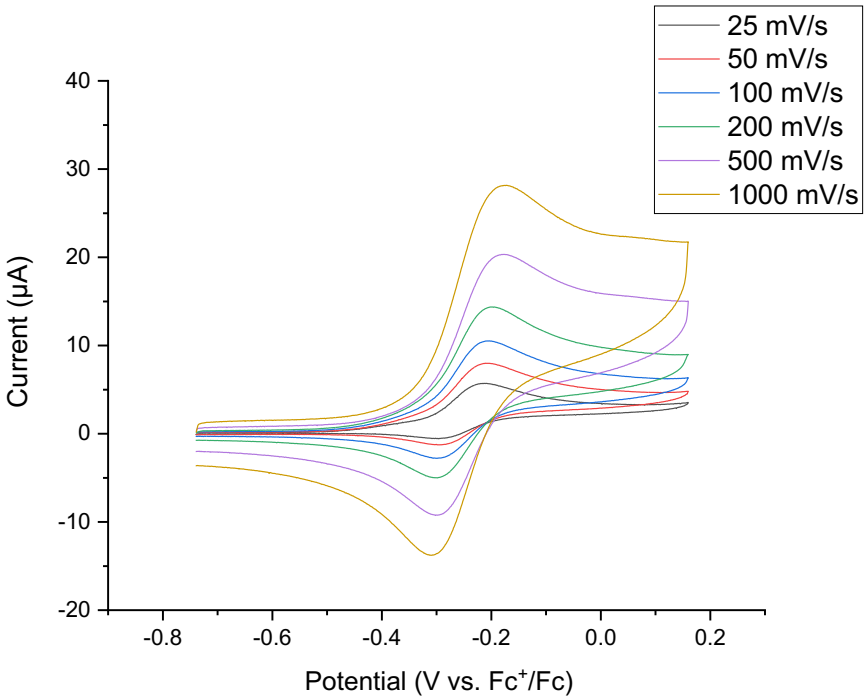

Figure S2. Cyclic voltammogram of [Bu_4N][**1**] (a) and [Bu_4N][**2**] (b) (1mM) in THF (0.1 M Bu_4NPF_6).

4. Titration data

(a)

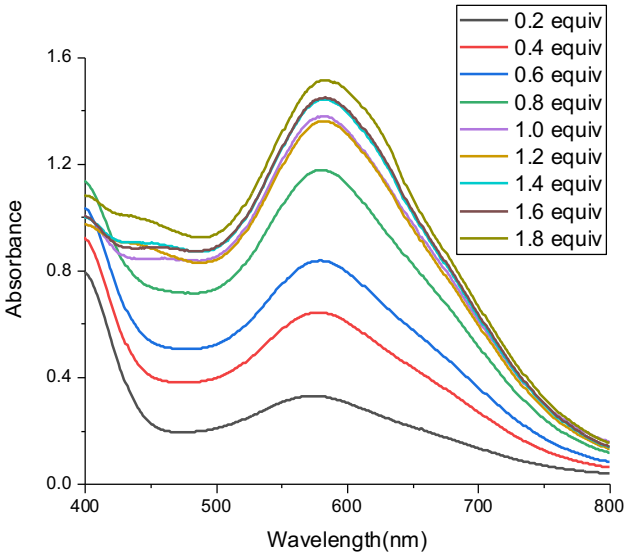

(b)

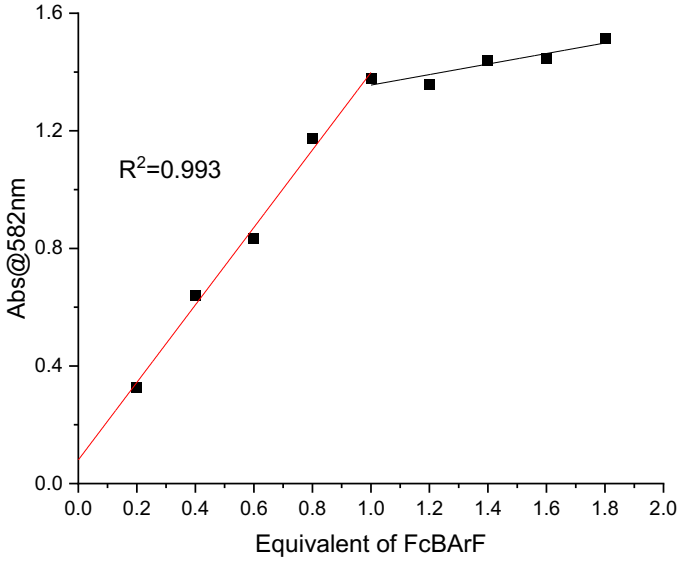

Figure S3. Titration data for reaction of [Bu_4N][**1**] with $FcBAr^F$ at −80 °C in THF. [Cu] = 0.2mM (a) UV-vis spectra as different equivalents of $FcBAr^F$ are added to the [Bu_4N][**1**] solution. (b) Absorbance at 582 nm as a function of equivalent oxidant added to the solution.

(a)

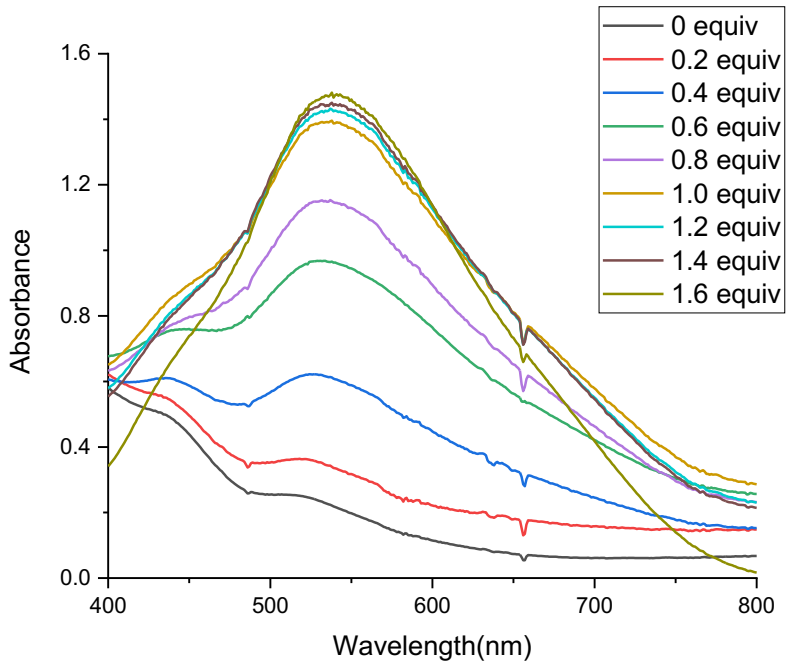

(b)

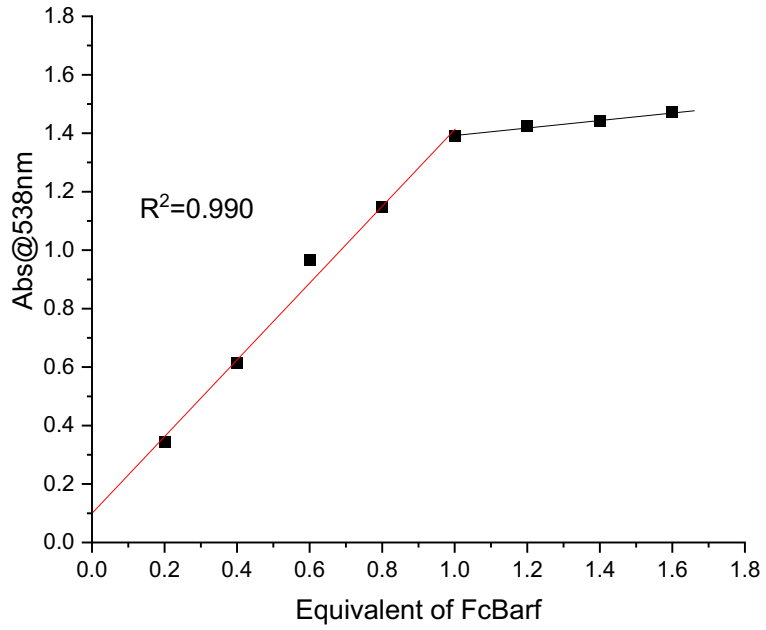

Figure S4. Titration data for reaction of [Bu_4N][**2**] with $FcBAr^F$ at −80 °C in THF. [Cu] = 0.1mM (a) UV-vis spectra as different equivalents of $FcBAr^F$ are added to the [Bu_4N][**2**] solution. (b) Absorbance at 538 nm as a function of equivalent oxidant added to the solution.

5. UV-Vis spectra of the reversible redox reactions

(a)

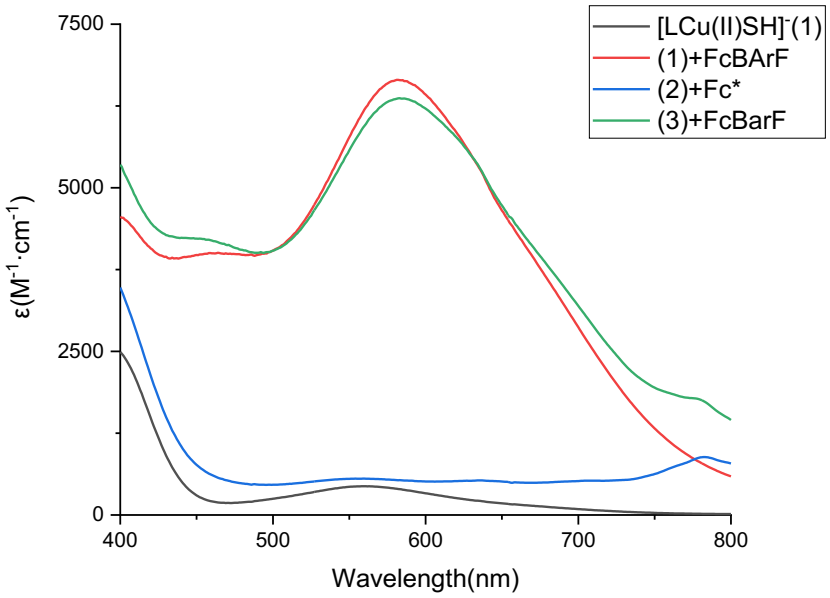

(b)

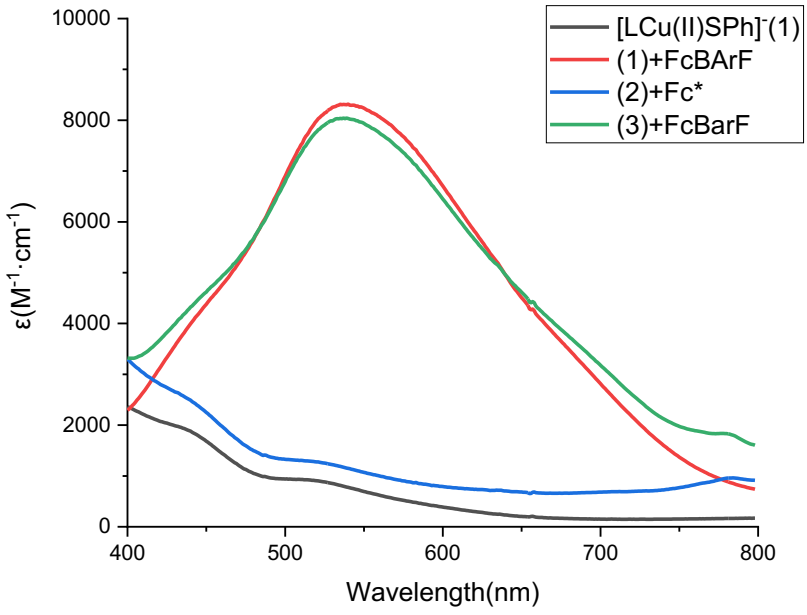

Figure S5. UV-Vis spectra of the reversible redox reactions of [Bu_4N][**1**] (a) and [Bu_4N][**2**] (b) at −80 °C in THF: oxidation with $FcBAr^F$ and subsequent reduction with Fc*.

6. EPR spectrum of sample made from reaction of LCuSH with TEMPOH (frequency 9.376 GHz).

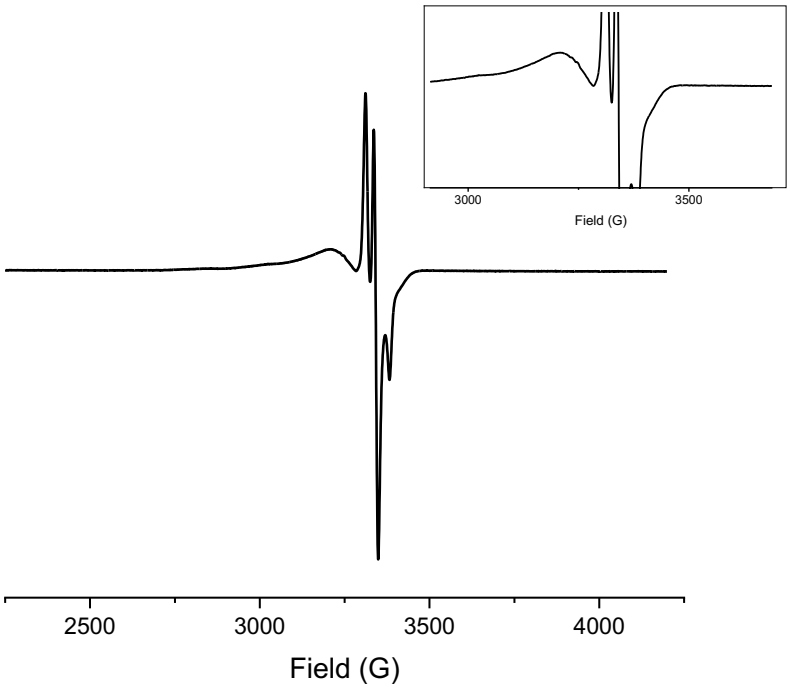

Figure S6. EPR spectrum of samples made from reaction between compound LCuSH (prepared by reaction of $[Bu_4N][\mathbf{1}]$ with $FcBAr^F$) and 10 equiv. of TEMPOH. Inset shows a zoomed view indicating features derived from Cu(II) species.

7. Reactivity plots for reactions of $LCu^{III}SH$ and $LCu^{III}SPh$ with TEMPOH

(a)

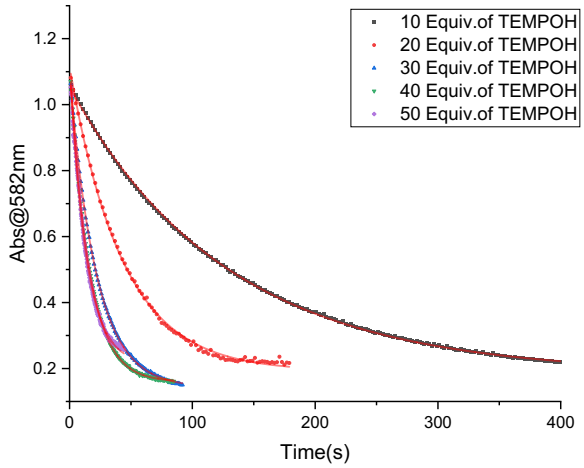

(b)

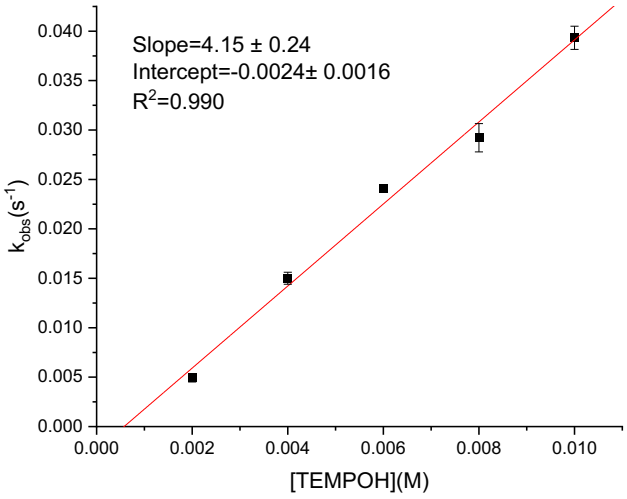

Figure S7. (a) Plots of Absorbance at 582 nm vs. time for representative reactions of LCuSH with different concentrations of TEMPOH at -80 °C. All reactions were run in duplicate or triplicate. Each decay trace was fit to a single exponential decay function shown as red lines (b) Plot of observed rate constants (k_{obs}) for the reaction of LCuSH with different concentrations of TEMPOH. Standard error from the data shown as bars.

(a)

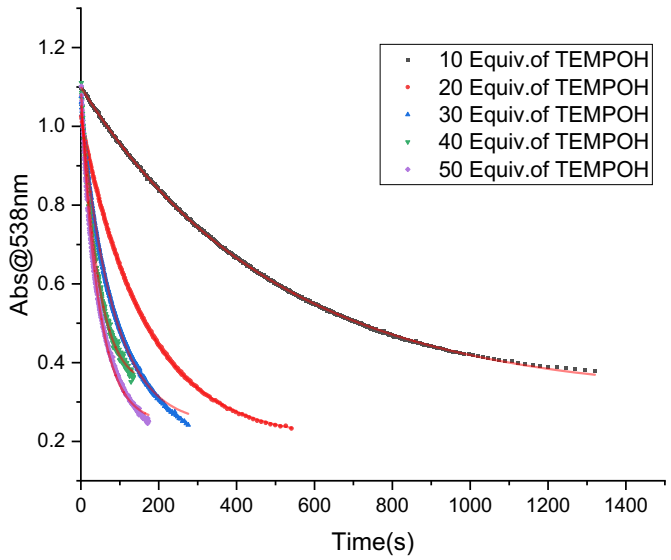

(b)

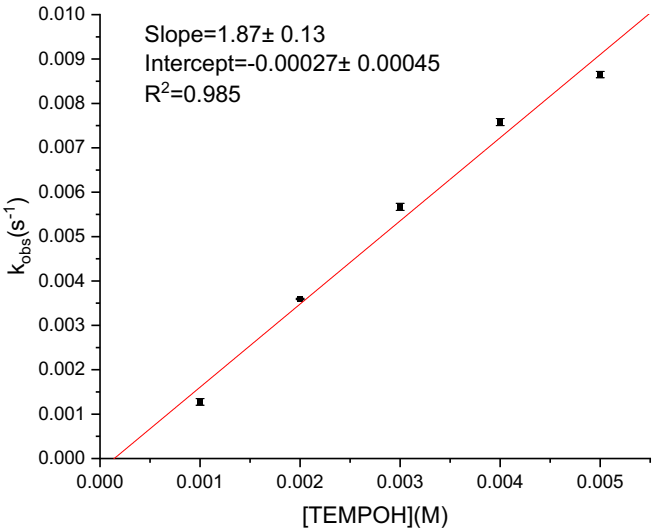

Figure S8. (a) Plots of Absorbance at 538 nm vs. time for representative reactions of LCuSPh with different concentrations of TEMPOH at -80 °C. All reactions were run in duplicate or triplicate. Each decay trace was fit to a single exponential decay function shown as red lines (b) Plot of observed rate constants (k_{obs}) for the reaction of LCuSPh with different concentrations of TEMPOH. Standard error from the data shown as bars.

8. Eyring plots for reactions of $LCu^{III}SH$ and $LCu^{III}SPh$ with TEMPOH

(a)

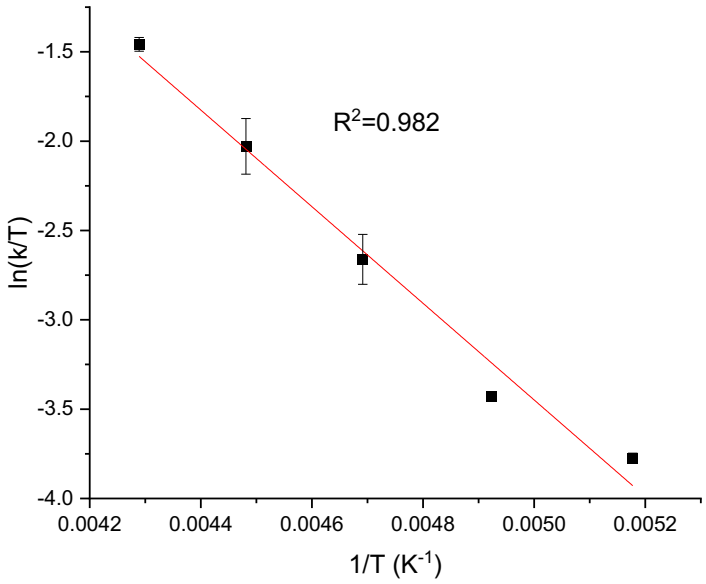

(b)

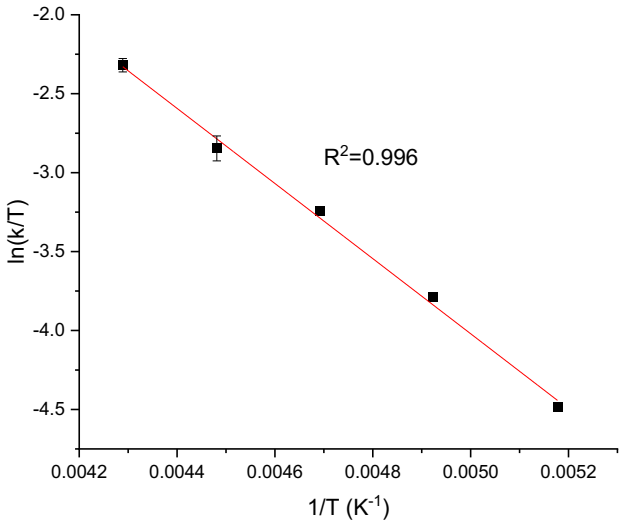

Figure S9. Plots of ln(k/T) vs 1/T (where k = second-order rate constant, T = temperature in K) for the reaction of LCuSH (a) or LCuSPh (b) with TEMPOH. The shown linear fits were used to calculate the activation parameters using the Eyring equation. Standard error from the data shown as bars. Derived activation parameters are reported in the text.

9. Computational details

Gas phase geometry optimizations were performed for the ground state singlet using the mPW1PW91[6] functional as implemented in Gaussian 16.[7] The Stuttgart basis set[8] and pseudopotential were used for Cu while the remaining atoms were treated with the 6-311+G(d,p) basis set. Each structure was confirmed as a minimium by harmonic vibrational analysis. Singlet states of all complexes were located without imposing symmetry with the OH and SH group coplanar to the ligand. Single point calculations were performed for the triplet states on the singlet geometries. Time-dependent DFT (TDDFT) calculations were also performed using the hybrid B98[9] functional in Gaussian 16 with the same basis sets as in the optimization. UV-Vis transition energies were computed for the first 36 states for the singlet wavefunction. These transitions were fitted to standard Gaussian curves to determine the calculated spectra with a broadening value of 0.333 eV.

To assess the multiconfigurational character of ^{CH3}LCuX complexes (X = OH, SH, Br, Cl, and F), additional calculations were performed using wavefunction based methods. First, multireference complete active space (CASSCF)[10] calculations were performed on the DFT optimized geometries using the OpenMolcas V18.09 program package.[11] Scalar relativistic effects were included using the second order Douglas-Kroll-Hess (DHK) Hamiltonian[12] and relativistic atomic natural orbital (ANO-RCC) type basis sets.[13] The copper, nitrogen, and X ligand were treated with the triple-ζ quality basis sets, while peripheral carbon, oxygen, and hydrogen atoms were treated with double-ζ quality basis sets. Specifically, the contractions used are 6s5p3d2f1g for copper, 4s3p2d1f for nitrogen, 5s4p2d1f for sulfur, 3s2p1d (or 4s3p2d1f) for oxygen, 4s3p2d1f for fluorine, 5s4p2d1f for chlorine, 6s4p3d2f1g for bromine, 3s2p1d for carbon, and 2s1p for hydrogen. Hirshfeld percent atomic contributions to the active natural orbitals and Bader's

quantum theory of atoms in molecules (QTAIM) analyses were performed as implemented in the MultiWFN program package.[14] Cholesky[17] decomposition in combination with local-exchange screening was used to decrease the computational cost associated with computing the two electron integrals. The second type of wavefunction-based calculation used to assess the multiconfigurational character of the LCuX complexes is the DLPNO-CCSD[18] as implemented in the Orca program package Version 4.2.1.[19] The def2-TZVP basis set was used on all atoms along with the resolution of the identity approximation. When the T1 diagnostic value is larger than 0.020, the complex is considered to be multiconfigurational.[20] Note that for X = Br, Cl, and F, DLPNO-CCSD calculations were performed on structures taken from ref. 21 and are ^{H}LCuX complexes.

10. DFT optimized geometric parameters and calculated energy difference data

Table S2. DFT optimized geometric parameters for the ^{R}LCuX.

	^{CH3}**LCuOH**	^{iPr}**LCuOH**	^{CH3}**LCuSH**	^{iPr}**LCuSH**	^{CH3}**LCuBr**	^{CH3}**LCuCl**	^{CH3}**LCuF**
Cu-X	1.78	1.78	2.16	2.16	2.27	2.13	1.77
X-H	0.96	0.96	1.35	1.35	-	-	-
Cu-N1	1.85	1.85	1.88	1.88	1.87	1.86	1.84
Cu-N2	1.92	1.92	1.93	1.93	1.95	1.94	1.92
Cu-N3	1.91	1.91	1.93	1.93	1.95	1.94	1.92
N1-Cu-X	177.05	177.16	176.67	176.71	179.97	179.99	180.0
N2-Cu-N3	166.51	166.45	165.73	165.70	165.02	165.37	166.72

Table S3. Calculated (mPW1PW91) energy differences between the S=0 and S=1 states for ^{R}LCuX complexes in kcal/mol.

	Singlet-Triplet Splitting (kcal/mol)
^{CH3}LCuOH	28.61
^{iPr}LCuOH	31.33
^{CH3}LCuSH	22.69
^{iPr}LCuSH	21.53
^{CH3}LCuSPh	20.08
^{iPr}LCuSPh	19.33
^{CH3}LCuBr	15.97
^{CH3}LCuCl	18.55
^{CH3}LCuF	18.44

11. UV-vis data obtained from TDDFT studies

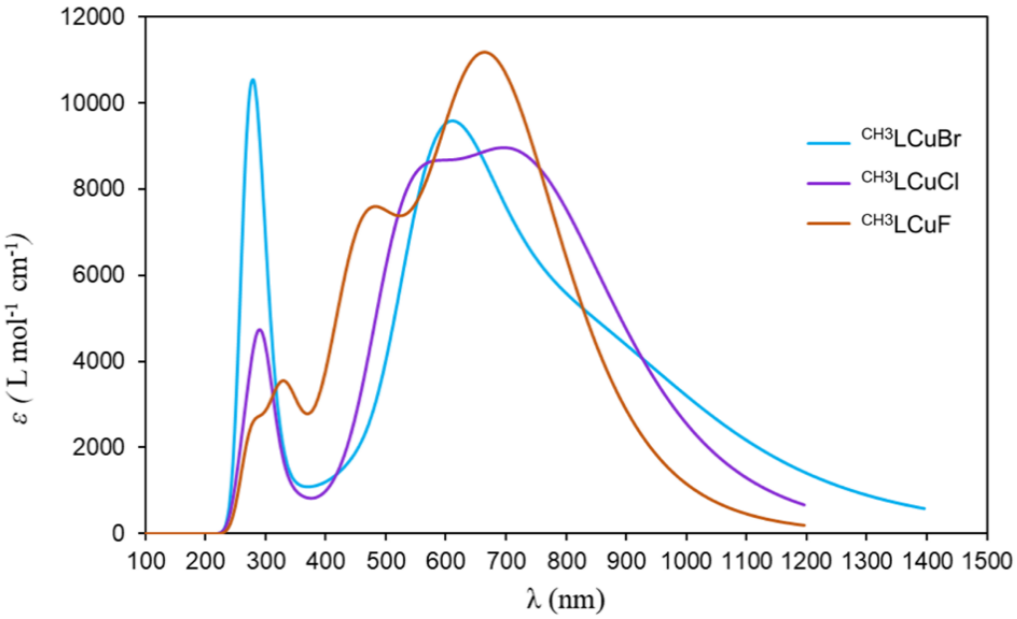

Figure S10. UV-Vis spectra of ^{CH3}Cu-X for X=Br, Cl, F computed at the B98/6-11+G(d,p)/SDD level of theory with a spectral broadening value of 0.333 eV

Table S4. UV-vis data obtained from TDDFT studies of complexes computed at the TD-B98/6-311+G(d,p)/SDD level of theory.

Complex	Energy (nm)	Oscillator Strength	Description	Coefficients
^{CH3}LCu-OH	552.70	0.208	LMCT (HOMO to LUMO	0.5227
^{iPr}LCu-OH	546.09	0.319	LMCT (HOMO to LUMO	0.6961
^{CH3}LCu-SH	613.12	0.210	LMCT (HOMO to LUMO	0.7003
^{iPr}LCu-SH	620.86	0.206	LMCT (HOMO to LUMO	0.7003
^{CH3}LCu-SPh	448.88	0.1867	LMCT (HOMO-5 to LUMO)	0.4134
^{iPr}LCu-SPh	465.23	0.2577	LMCT (HOMO-4 to LUMO)	0.4012
			LMCT (HOMO-5 to LUMO)	0.4613
	619.83	0.1816	LMCT (HOMO to LUMO)	0.5563
^{CH3}LCu-F	676.56	0.249	LMCT (HOMO to LUMO)	0.6779
	505.51	0.090	LMCT (HOMO-6 to LUMO)	0.5925
^{CH3}LCu-Cl	745.95	0.191	LMCT (HOMO to LUMO)	0.6675
	553.14	0.135	LMCT (HOMO-6 to LUMO)	0.5169
^{CH3}LCu-Br	861.85	0.0857	LMCT (HOMO to LUMO)	0.6303
	608.34	0.199	LMCT (HOMO-4 to LUMO)	0.5766
	274.01	0.203	LMCT (HOMO-12 to LUMO)	0.5797

12. Selected molecular orbitals from the complexes

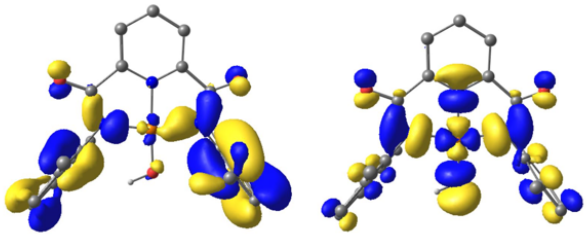

Figure S11. Selected molecular orbitals from the ^{CH3}LCuOH structure computed at the *m*PW1PW91/6-311+G(d,p)/SDD level of theory. Orbitals are plotted with an isovalue of 0.03 a.u. Hydrogen atoms, with the exception of the OH group, are excluded for clarity. C in grey, Cu in orange, O in red, N in blue, and H in white

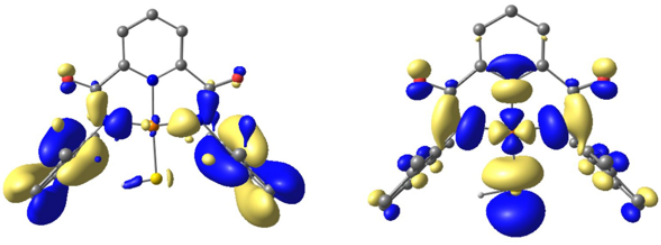

HOMO LUMO

Figure S12. Selected molecular orbitals from the ^{CH3}LCuSH structure computed at the *m*PW1PW91/6-311+G(d,p)/SDD level of theory. Orbitals are plotted with an isovalue of 0.03 a.u. Hydrogen atoms, with the exception of the SH group, are excluded for clarity. C in grey, Cu in orange, O in red, N in blue, S in yellow and H in white

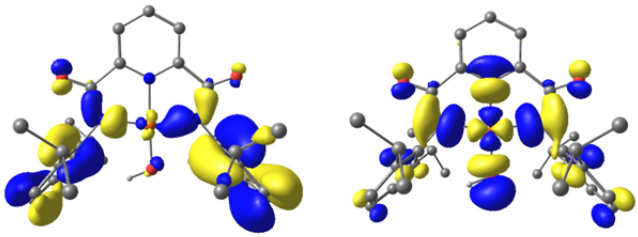

HOMO LUMO

Figure S13. Selected molecular orbitals from the ^{iPr}LCuOH structure computed at the *m*PW1PW91/6-311+G(d,p)/SDD level of theory. Orbitals are plotted with an isovalue of 0.03 a.u. Hydrogen atoms, with the exception of the OH group, are excluded for clarity. C in grey, Cu in orange, O in red, N in blue, and H in white

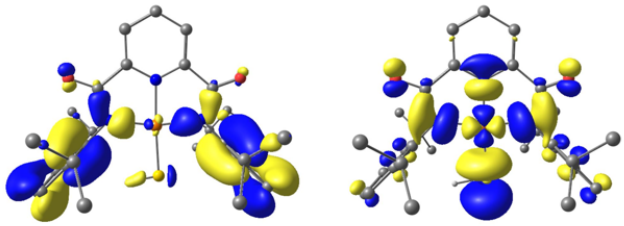

HOMO LUMO

Figure S14. Selected molecular orbitals from the ^{iPr}LCuSH structure computed at the *m*PW1PW91/6-311+G(d,p)/SDD level of theory. Orbitals are plotted with an isovalue of 0.03 a.u. Hydrogen atoms, with the exception of the SH group, are excluded for clarity. C in grey, Cu in orange, O in red, N in blue, S in yellow and H in white

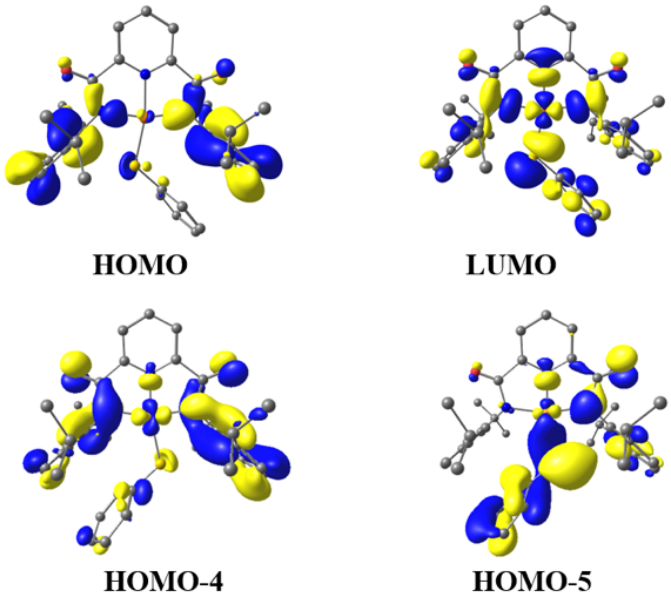

Figure S15. Selected molecular orbitals from the ^{iPr}LCuSPh structure computed at the *m*PW1PW91/6-311+G(d,p)/SDD level of theory. Orbitals are plotted with an isovalue of 0.03 a.u. Hydrogen atoms are excluded for clarity. C in grey, Cu in orange, O in red, N in blue, and S in yellow

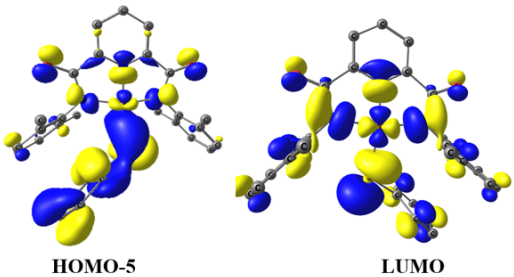

Figure S16. Selected molecular orbitals from the ^{CH3}LCuSPh structure computed at the *m*PW1PW91/6-311+G(d,p)/SDD level of theory. Orbitals are plotted with an isovalue of 0.03 a.u. Hydrogen atoms are excluded for clarity. C in grey, Cu in orange, O in red, N in blue, S in yellow.

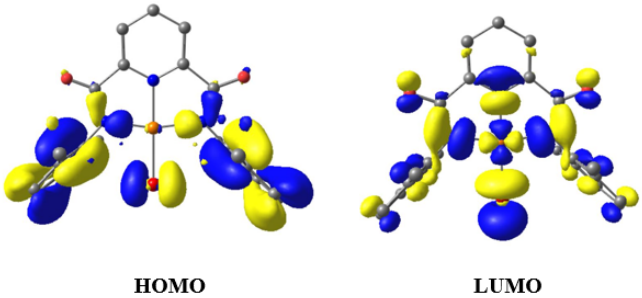

Figure S17. Selected molecular orbitals from the ^{CH3}LCuBr structure computed at the *m*PW1PW91/6-311+G(d,p)/SDD level of theory. Orbitals are plotted with an isovalue of 0.03 a.u. Hydrogen atoms are excluded for clarity. C in grey, Cu in orange, O in red, N in blue, and Br bright red.

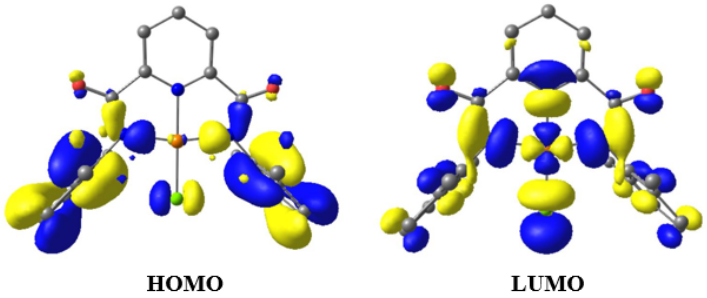

Figure S18. Selected molecular orbitals from the ^{CH3}LCuCl structure computed at the *m*PW1PW91/6-311+G(d,p)/SDD level of theory. Orbitals are plotted with an isovalue of 0.03 a.u. Hydrogen atoms are excluded for clarity. C in grey, Cu in orange, O in red, N in blue, Cl in green.

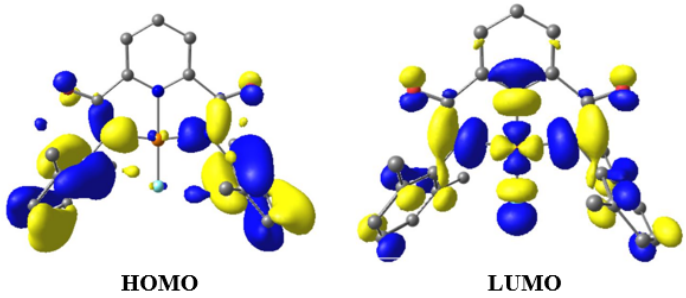

Figure S19. Selected molecular orbitals from the ^{CH3}LCuF structure computed at the *m*PW1PW91/6-311+G(d,p)/SDD level of theory. Orbitals are plotted with an isovalue of 0.03 a.u. Hydrogen atoms are excluded for clarity. C in grey, Cu in orange, O in red, N in blue, and F in cyan.

13. CASSCF active space validation

A larger active space that includes additional π orbitals on the ligand was tested to validate the choice of the minimal (2*e*,2*o*) active space. The (12*e*,12*o*) active space yielded results in excellent agreement with the smaller active space (Figures S11-S15), supporting the choice of active space presented in the manuscript. Specifically, the larger active space consists of 12 orbitals containing 12 electrons which includes the σ and σ* orbitals in addition to set of five π and π* orbitals. CASSCF natural orbitals for the (2*e*,2*o*) active space are shown in Figure 4.

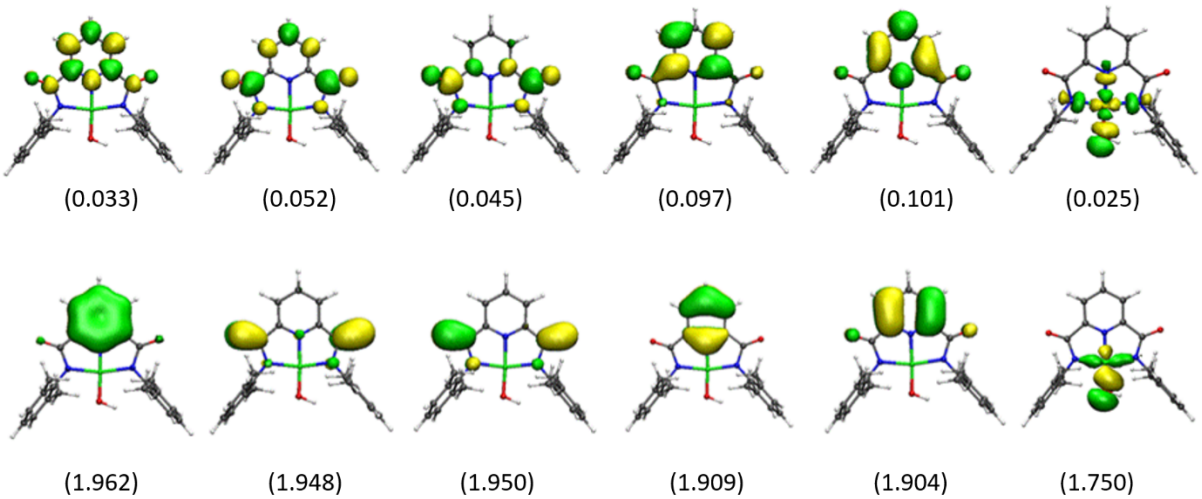

Figure S20. CASSCF natural orbitals from the (12*e*, 12*o*) calculation for ^{CH3}LCuOH. Orbitals are shown at an isovalue of 0.04 a.u.

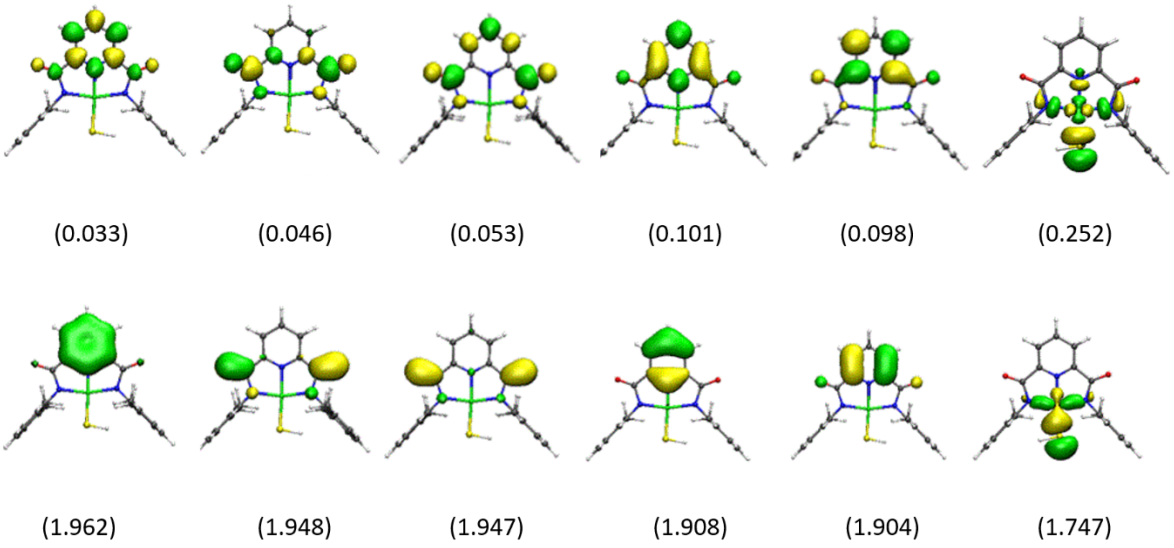

Figure S21. CASSCF natural orbitals from the (12*e*, 12*o*) calculation for ^{CH3}LCuSH. Orbitals are shown at an isovalue of 0.04 a.u.

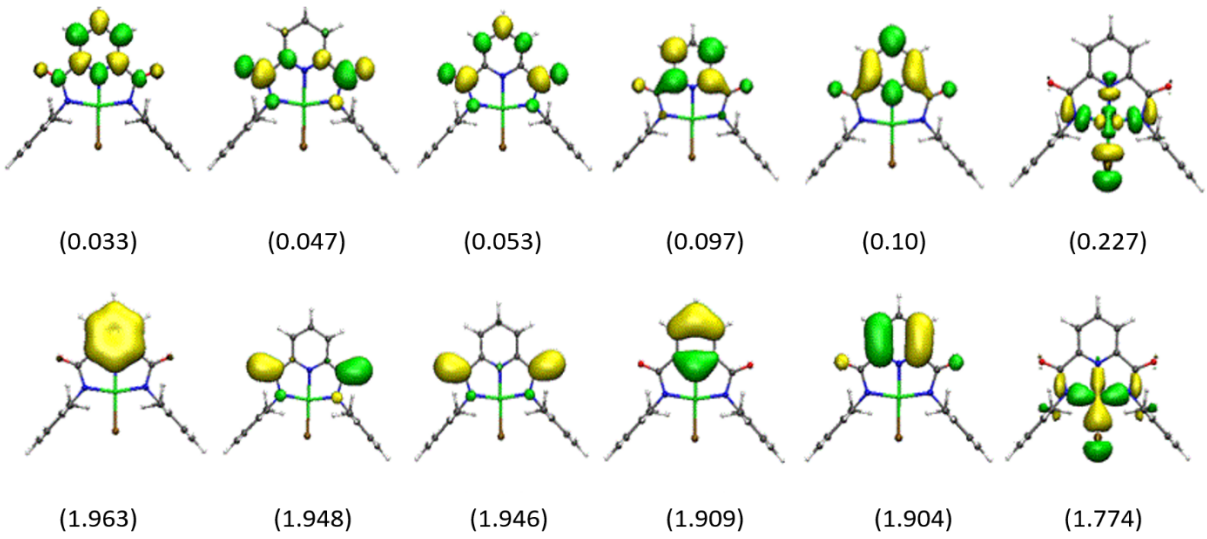

Figure S22. CASSCF natural orbitals from the (12*e*, 12*o*) calculation for ^{CH3}LCuBr. Orbitals are shown at an isovalue of 0.04 a.u.

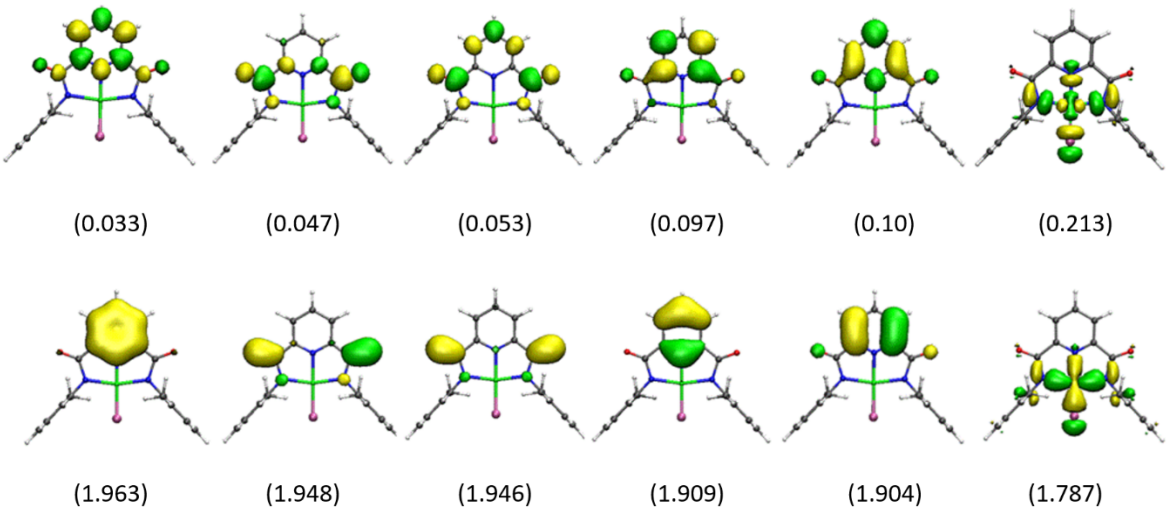

Figure S23. CASSCF natural orbitals from the (12*e*, 12*o*) calculation for ^{CH3}LCuCl. Orbitals are shown at an isovalue of 0.04 a.u.

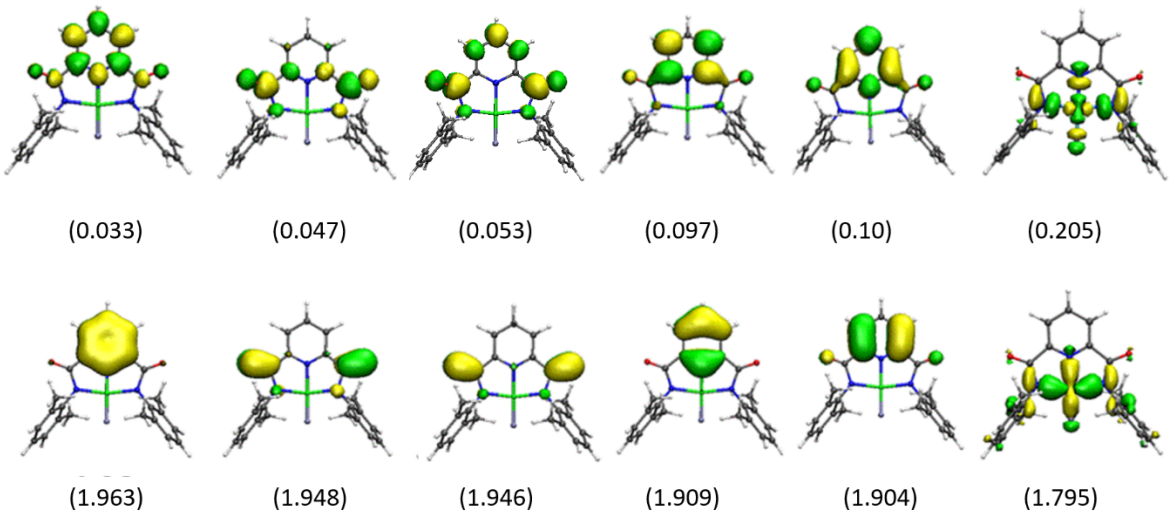

Figure S24. CASSCF natural orbitals from the (12*e*, 12*o*) calculation for ^{CH3}LCuF. Orbitals are shown at an isovalue of 0.04 a.u.

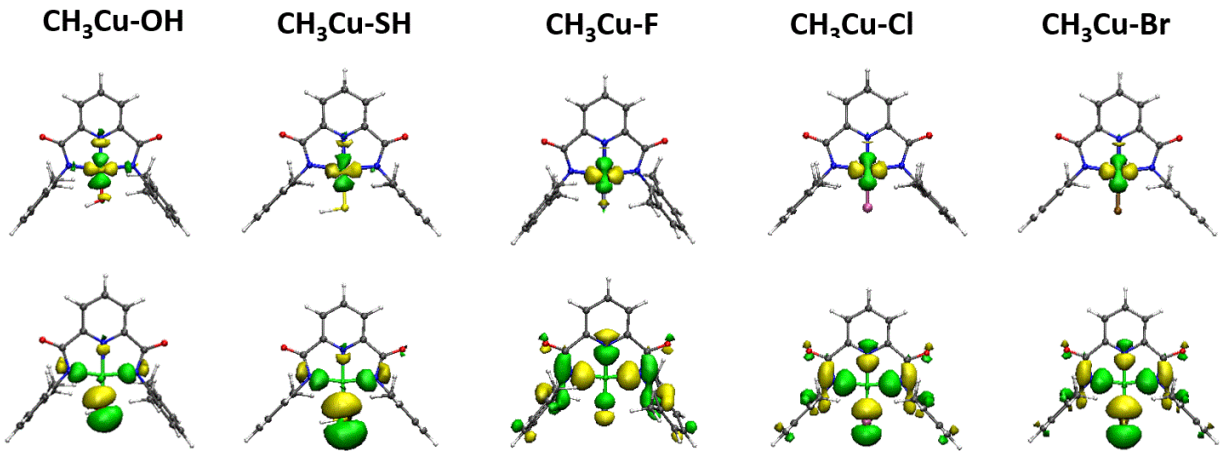

Figure S25. Cholesky localized orbitals used in the CAS-CI (2*e*,2*o*) calculations for ^{CH3}LCuX complexes. Orbitals are shown at an isovalue of 0.04 a.u.

14. Localized orbital CAS-CI results

The localized orbital CAS-CI approach consists of recomputing the CASSCF CI coefficients after localizing the active orbitals. CASSCF is invariant with respect to unitary transformations of the active orbitals. Therefore, the CASSCF solution and the localized orbital CAS-CI solution are energetically equivalent.

Localized Orbital CAS-CI of Ethene.

To better understand the valence-bond like interpretation of CASSCF approach we performed calculation for ethene. A two electron in two orbital CASSCF calculation (2*e*,2*o*) including the π and π* orbitals results in occupation numbers of 1.89 and 0.11, respectively (Figure S26). The major configuration contributing towards the wavefunction can be represented as $\pi^2\pi^{*0}$ (94.2%) followed by the $\pi^0\pi^{*2}$ (5.7%) (Table S5). However, performing a projected atomic orbital (PAO) localization on these active orbitals and subsequent CAS-CI calculations (Figure S26) results in the following configurations: $p_1^2p_2^{*0}$ (13.4%), $p_1^0p_2^{*2}$ (13.4%), $p_1^1p_2^{*1}$ (73.3%) (Table S5). Although the CASSCF and localized orbital CAS-CI energies are equal, the resulting wavefunction is clearly different for the two calculations.

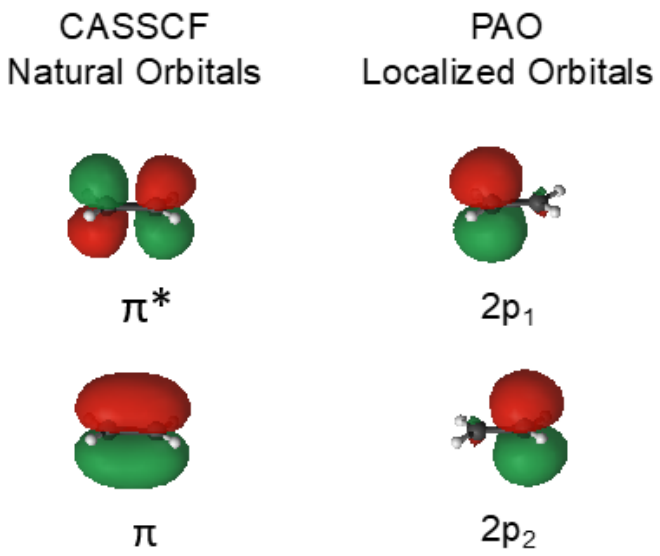

Figure S26. CASSCF natural orbitals (left) before localization and the PAO localized orbitals (right) used in the localized orbital CAS-CI calculation for ethylene. Orbitals are shown at an isovalue of 0.04**.**

Table S5. Percent contributions of the configurations involved in both the CASSCF and localized orbital CAS-CI wavefunctions calculation for ethylene.

Method	Configuration	Contribution
CASSCF	$\pi^2\pi^{*0}$	94.2%
	$\pi^0\pi^{*2}$	5.7%
	$\pi^1\ \pi^{*1}$	0.0%
localized orbital CAS-CI	$p_1^2p_2^0$	13.3%
	$p_1^0p_2^2$	13.3%
	$p_1^1p_2^1$	73.3%

CASSCF and Localized Orbital CAS-CI of ^{H}LCuX (X = F, Cl, Br) with Different Localization Schemes and Software Packages

Table S6. Percent contributions to the CASSCF wavefunction using Orca (computational details as described by Bower et al.) and OpenMolcas (computational details as described in this work). Geometry taken from ref. 21.

Software	Complex	$\sigma^2\sigma^{*0}$	$\sigma^0\sigma^{*2}$	$\sigma^1\sigma^{*1}$
Orca	^{H}LCuF	92.0	8.0	0
	^{H}LCuCl	90.9	9.1	0
	^{H}LCuBr	89.7	10.3	0
OpenMolcas	^{H}LCuF	92.0	8.0	0
	^{H}LCuCl	91.0	9.0	0
	^{H}LCuBr	89.8	10.2	0

Table S7. Localized orbital CAS-CI results using Orca (computational details as described by Bower et al.) with three different localization schemes (IAO-BOYS, IAO-IBO, and PM). Geometry taken from ref. 21.

Localization Scheme	Complex	$d^2(LX)^0$ (Cu^IX^+)	$d^0(LX)^2$ ($Cu^{III}X^-$)	$d^1(LX)^1$ ($Cu^{II}X^{\cdot}$)
IAO-BOYS	^{H}LCuF	0	51.9	47.9
	^{H}LCuCl	2.1	25.7	72.2
	^{H}LCuBr	2.7	21.5	75.8
IAO-IBO	^{H}LCuF	11.3	11.6	77.1
	^{H}LCuCl	12.8	8.7	78.5
	^{H}LCuBr	12.6	7.4	80.0
PM	^{H}LCuF	11.3	11.6	77.1
	^{H}LCuCl	12.1	9.2	78.6
	^{H}LCuBr	12.1	7.8	80.1

Table S8**.** Localized orbital CAS-CI results using OpenMolcas (computational details as described in this work) with four different localization schemes (Cholesky, Boys, PM, and PAO). Geometry taken from ref. 21.

Localization Scheme	Complex	$d^2(LX)^0$ (Cu^IX^+)	$d^0(LX)^2$ ($Cu^{III}X^-$)	$d^1(LX)^1$ ($Cu^{II}X^{\cdot}$)
Cholesky	^{H}LCuF	5.1	20.4	74.5
	^{H}LCuCl	6.9	15.2	77.8
	^{H}LCuBr	7.1	13.0	19.8
Boys	^{H}LCuF	50.6	0.1	49.3
	^{H}LCuCl	25.8	2.1	72.1
	^{H}LCuBr	21.0	2.9	76.1
PM	^{H}LCuF	12.5	10.5	77.1
	^{H}LCuCl	11.6	9.8	78.6
	^{H}LCuBr	11.5	8.3	80.2

15. Orbital composition

Table S9. Percent contributions to the molecular orbitals (CASSCF or Cholesky localized) computed by Hirshfeld analysis as implemented in MultiWFN.

		CASSCF σ	**CASSCF σ***	**CAS-CI d**	**CAS-CI LZ**
F	Cu	47.9	53.1	94.6	6.3
	F	3.6	5.6	1.0	8.1
	L	48.6	41.3	4.3	85.6
Cl	Cu	50.1	51.1	95.0	6.5
	Cl	11.3	11.5	1.1	21.7
	L	38.6	36.9	3.9	71.8
Br	Cu	51.2	50.7	95.0	6.9
	Br	18.3	16.5	1.2	33.6
	L	30.5	32.8	3.8	59.5
OH	Cu	46.1	50.4	90.5	6.07
	OH	48.6	33.9	3.0	79.4
	L	5.3	15.7	6.5	14.5
SH	Cu	52.6	49.6	93.1	9.1
	SH	38.1	31.2	2.0	67.3
	L	9.3	19.2	4.9	23.6

16. QTAIM analysis calculations on the CASSCF results

In QTAIM theory, a chemical bond exists if a line of locally maximum electron density, ρ, joins two neighboring atoms and a bond critical point (BCP) exists (a minimum in the density). At the BCP, the gradient of the electron density is zero while the Laplacian, $\nabla\rho^2$, may have either a net positive or negative value. A positive Laplacian suggests a local depletion of charge, while a negative value is a sign of a local concentration of charge. The latter is a strong condition for a covalent bond, while a "closed-shell" interaction is associated with a positive Laplacian. Since there exists a continuum between a covalent and a non-covalent bond, Bianchi *et al.*[22] suggested classifying of the bond between two "closed shell" interacting atoms by introducing a second condition, the total electronic energy density at the BCP, E(r). This term is defined as the sum of

the kinetic energy density, G(r), which usually dominates in a non-covalent bond, and the potential energy density V (r),which is usually negative and associated with an accumulation of charge between the nuclei. In clear covalent bonds both the Laplacian and E(r) are negative. In less clear cases, where the Laplacian is slightly positive, the value of E(r) can be used to make a further classification of the bond, from being slightly covalent to purely ionic/nonbonded. In this classification, with $\nabla\rho^2>0$, if E(r) is negative, the bond is called dative; if E(r) close to zero, the bond is metallic; if E(r) is positive, the bond can be either ionic or van der Waals. Following these rules, the complexes included in Table S10 would all be classified as dative.

Table S10**.** Parameters from the quantum theory of atoms in molecules (QTAIM) analysis calculations on the CASSCF results. If $\nabla^2(\rho) > 0$ and $E(r) < 0$, the bond is considered to be dative.

	$\nabla^2(\rho)$, (bohr)	**E(r) (bohr)**	**G(r) (a.u.)**	**V(r) (a.u.)**
^{CH3}LCuOH	0.5145	-0.0523	0.1809	-0.2333
^{CH3}LCuSH	0.1009	-0.0417	0.0669	-0.1087
^{CH3}LCuBr	0.1401	-0.0303	0.0653	-0.0956
^{CH3}LCuCl	0.2452	-0.0370	0.0983	-0.1353
^{CH3}LCuF	0.8010	-0.0368	0.2370	-0.2738

17. DLPNO-CCSD results

Table S11. T1 diagnostic values computed with DLPNO-CCSD. Values less than 0.02 indicate that there is not significant multiconfigurational character. Geometry taken from ref. 20.

Complex	**T1 Diagnostic**
^{H}LCuF	0.01878
^{H}LCuCl	0.01788
^{H}LCuBr	0.01686
^{CH3}LCuOH	0.01781
^{CH3}LCuSH	0.01639

18. Reference

1. Donoghue, P. J.; Tehranchi, J.; Cramer, C. J.; Sarangi, R.; Solomon, E. I.; Tolman, W. B., Rapid C–H Bond Activation by a Monocopper(III)–Hydroxide Complex, *J. Am. Chem. Soc.* **2011**, *133*, 17602-17605
2. Hartle, M. D.; Meininger, D. J.; Zakharov, L. N.; Tonzetich, Z. J.; Pluth, M. D., NBu_4 SH provides a convenient source of HS^- soluble in organic solution for H_2S and anion-binding research. *Dalton Trans.* **2015,** *44*, 19782-19785.
3. Mader, E. A.; Davidson, E. R.; Mayer, J. M., Large ground-state entropy changes for hydrogen atom transfer reactions of iron complexes. *J. Am. Chem. Soc.* **2007,** *129*, 5153-5166.
4. Le Bras, J.; Jiao, H.; Meyer, W. E.; Hampel, F.; Gladysz, J. A., Synthesis, crystal structure, and reactions of the 17-valence-electron rhenium methyl complex [(η^5-C_5Me_5) Re(NO)(P(4-$C_6H_4CH_3)_3$)(CH_3)]$^+$B(3,5-$C_6H_3(CF_3)_2)^{4-}$: Experimental and computational bonding comparisons with 18-electron methyl and methylidene complexes. *J. Organomet. Chem.* **2000,** *616*, 54-66
5. (a) Gagne, R. R.; Koval, C. A.; Lisensky, G. C. Ferrocene as an internal standard for electrochemical measurements. *Inorg. Chem*. **1980**, *19*, 2854-2855. (b) Connelly, N. G., Geiger, W. E. Chemical redox agents for organometallic chemistry. *Chem. Rev.* **1996**, *96*, 877-910.
6. Adamo, C.; Barone, V. Exchange functionals with improved long-range behavior and adiabatic connection methods without adjustable parameters: The mPW and mPW1PW models. *J. Chem. Phys.* **1998**, *108***,** 664-675.
7. Gaussian 16, Revision A.03, M. J. Frisch, G. W. Trucks, H. B. Schlegel, G. E. Scuseria, M. A. Robb, J. R. Cheeseman, G. Scalmani, V. Barone, G. A. Petersson, H. Nakatsuji, X. Li, M. Caricato, A. V. Marenich, J. Bloino, B. G. Janesko, R. Gomperts, B. Mennucci, H. P. Hratchian, J. V. Ortiz, A. F. Izmaylov, J. L. Sonnenberg, D. Williams-Young, F. Ding, F. Lipparini, F. Egidi, J. Goings, B. Peng, A. Petrone, T. Henderson, D. Ranasinghe, V. G. Zakrzewski, J. Gao, N. Rega, G. Zheng, W. Liang, M. Hada, M. Ehara, K. Toyota, R. Fukuda, J. Hasegawa, M. Ishida, T. Nakajima, Y. Honda, O. Kitao, H. Nakai, T. Vreven, K. Throssell, J. A. Montgomery, Jr., J. E. Peralta, F. Ogliaro, M. J. Bearpark, J. J. Heyd, E. N. Brothers, K. N. Kudin, V. N. Staroverov, T. A. Keith, R. Kobayashi, J. Normand, K. Raghavachari, A. P. Rendell, J. C. Burant, S. S. Iyengar, J. Tomasi, M. Cossi, J. M. Millam, M. Klene, C. Adamo, R. Cammi, J. W. Ochterski, R. L. Martin, K. Morokuma, O. Farkas, J. B. Foresman, and D. J. Fox, Gaussian, Inc., Wallingford CT, 2016.
8. Dolg, M.; Wedig, U.; Stoll, H.; Preuss, H. Energy-adjusted abinitio pseudopotentials for the first row transition elements. *J. Chem. Phys.* **1987**, *86*, 866-872.
9. Schmider, H. L.; Becke, A. D. Optimized density functionals from the extended G2 test set. *J. Chem. Phys.* **1998**, *108,* 9624-9631
10. (a) Andersson, K.; Malmqvist, P.-Å.; Roos, B. O.; Sadlej, A. J.; Wolinski, K. Second-order perturbation theory with a CASSCF reference function. *J. Phys. Chem.* **1990**, *94*, 5483–5488. (b) Andersson, K.; Malmqvist, P.-Å.; Roos, B. O. Second-order perturbation theory with a complete active space self-consistent field reference function. *J. Chem. Phys.* **1992**, *96*, 1218–1226.
11. Aquilante, F.; De Vico, L.; Ferre, N.; Ghigo, G.; Malmqvist, P.-Å.; Neogrady, P.; Pedersen, T. B.; Pitonak, M.; Reiher, M.; Roos, B. O.; Serrano-Andres, L.; Urban, M.; Veryazov, V.;

Lindh, R. MOLCAS 7: the next generation. *J. Comput. Chem.*, **2010**, *31*, 224–247.
12. B. A. Hess. Relativistic electronic-structure calculations employing a two-component no-pair formalism with external-field projection operators. *Phys. Rev. A*, **1986**, *33*, 3742–3748.
13. (a) Roos, B. O.; Lindh, R.; Malmqvist, P.-Å.; Veryazov, V.; Widmark, P.-O. Main group atoms and dimers studied with a new relativistic ANO basis set. *J. Phys. Chem. A.* **2004**, *108*, 2851–2858. (b) Roos, B. O.; Lindh, R.; Malmqvist, P.-A.; Veryazov, V.; Widmark, P.-O. New relativistic ANO basis sets for transition metal atoms. *J. Phys. Chem. A*, **2005**, *109*, 6575–6579.
14. Lu, T.; Chen, F. Multiwfn: a multifunctional wavefunction analyzer. *J. Comput. Chem.* **2012**, *33*, 580-592.
15. Ghigo, G.; Roos, B. O.;Malmqvist, P.-A . A modified definition of the zeroth-order Hamiltonian in multiconfigurational perturbation theory (CASPT2). *Chem. Phys. Lett.* **2004**, *396*, 142-149.
16. Forsberg, N.; Malmqvist, P-A. Multiconfiguration perturbation theory with imaginary level shift. *Chem Phys. Lett.*, **1997**, 274, 196-204.
17. (a) Aquilante, F.; Gagliardi, L.; Pedersen, T. B.; Lindh, R. Atomic Cholesky decompositions: A route to unbiased auxiliary basis sets for density fitting approximation with tunable accuracy and efficiency. *J. Chem. Phys.* **2009**, *130*, 154107. (b) Aquilante, F.; Lindh, R.; Pedersen, T. B. Analytic derivatives for the Cholesky representation of the two-electron integrals. *J. Chem. Phys.* **2008**, *129*, 034106. (c) Aquilante, F.; Malmqvist, P. A.; Pedersen, T. B.; Ghosh, A.; Roos, B. O. Cholesky Decomposition-Based Multiconfiguration Second-Order Perturbation Theory (CD-CASPT2): Application to the Spin-State Energetics of Co^{III}(diiminato)(NPh). *J. Chem. Theory Comput.* **2008**, *4*, 694–702.
18. Riplinger, C.; Neese, F. An efficient and near linear scaling pair natural orbital based local coupled cluster method. *J. Chem. Phys.* **2013**, *138*, 034106.
19. Neese, F. The ORCA program system, *Wiley Interdiscip. Rev.: Comput. Mol. Sci.*, **2012**, *2*, 73-78.
20. Lee, T. J.; Taylor, P. R. A diagnostic for determining the quality of single-reference electron correlation methods. *Int. J. Quant. Chem. Symp.* **1989**, *36(S23)*, 199–207
21. Bower, J. K.; Cypcar, A. D.; Henriquez, B.; Stieber, S. C. E.; Zhang, S. "C(sp^3)-H Fluorination with a Copper(II)/(III) Redox Couple", *J. Am. Chem. Soc.* **2020**, *142*, 8514–8521.
22. Bianchi, R; Gervasio, G; Marabello, B. Experimental Electron Density Analysis of $Mn_2(CO)_{10}$: Metal−Metal and Metal−Ligand Bond Characterization. *Inorg. Chem.* **2000**, *39*, 2360-2366